Available online at www.sciencedirect.com

ScienceDirect

journal homepage: www.elsevier.com/locate/issn/15375110

Research Paper

Field-based architectural traits characterisation of maize plant using time-of-flight 3D imaging

Yin Bao [a], Lie Tang [a,*], Srikant Srinivasan [b], Patrick S. Schnable [b]

[a] Department of Agricultural and Biosystems Engineering, Iowa State University, USA
[b] Department of Agronomy, Iowa State University, USA

ARTICLE INFO

Article history:
Received 21 May 2018
Received in revised form
31 October 2018
Accepted 6 November 2018

Keywords:
Maize
Plant phenotyping
Point cloud processing
Skeletonisation
Time-of-Flight

Maize (*Zea mays* L.) is one of the most economically important cereal crops. Though time-consuming and labour-intensive, manually measuring phenotypic traits in the field has been the common practice for maize breeding programs. This study presents a system for automated characterisation of several important plant architectural traits of maize plants under field conditions. An algorithm was developed to extract 3D plant skeletons from point cloud data acquired by side-viewing Time-of-Flight cameras. Plants were detected as 3D lines by Hough transform of the skeleton nodes. By analysing the graph structure of the skeletons with respect to the 3D lines, the point cloud was partitioned into plant instances with the stems and the leaves separated. Furthermore, plant height, plant orientation, leaf angle, and stem diameter were extracted for each plant. The image-derived estimates of traits were compared to manual measurements at multiple growth stages. Satisfactory accuracies in terms of mean absolute error (MAE) and coefficient of determination (R^2) were achieved for plant height (before flowering: MAE 0.15 m, R^2 0.96; after flowering: MAE 0.054 m, R^2 0.83), leaf angle (MAE 2.8°, R^2 0.83), and plant orientation (MAE 13°), except for stem diameter due to the limitations of the depth sensor. The results showed that the system was robust and accurate when the plants were imaged from only one side despite occlusions caused by leaves, and the method was applicable to maize plants from an early growth stage to full maturity.

Published by Elsevier Ltd on behalf of IAgrE.

1. Introduction

Maize (*Zea mays* L.) is one of the most economically important cereal crops worldwide for food, feedstock, fibre, and biofuel production. Rapid human population growth and climate change demand an acceleration in current breeding technologies for high-yield maize varieties. Though genotyping technologies are well developed, high-throughput plant phenotyping has been identified as the bottleneck to exploiting the extensive genomic data for crop improvement. Among various phenotypic traits, plant architecture determines a crop variety's capability to intercept light for photosynthesis, and thus yield. In fact, the increase in maize yield during the last decades largely resulted from the manipulation of plant architecture for adapting increased plant densities (Duvick, Smith, & Cooper, 2004), for instance, vertically oriented leaves above the ear and horizontally oriented leaves

* Corresponding author.
E-mail address: lietang@iastate.edu (L. Tang).
https://doi.org/10.1016/j.biosystemseng.2018.11.005
1537-5110/Published by Elsevier Ltd on behalf of IAgrE.

Nomenclature

c_x	The principal point along the camera X axis, pixel
c_y	The principal point along the camera Y axis, pixel
d	The depth value of a 2D image point, m
DAP	Days After Planting
f_x	The focal length along the camera X axis, pixel
f_y	The focal length along the camera Y axis, pixel
FOV	Field-Of-View, degree
LA	Leaf Angle, degree
MAE	Mean Absolute Error, m
PH	Plant Height, m
PO	Plant Orientation, degree
R^2	Coefficient of Determination, unitless
R_{collar}	A parameter for leaf skeleton segment identification, m
R_{plant}	A parameter for plant detection and segmentation, leaf skeleton segment identification, and plant orientation estimation, m
R_{stem}	A parameter for skeleton refinement, stem line detection, plant height estimation, leaf skeleton segment identification, and stem skeleton node identification, m
RGB-D	Red, Green, Blue, and Depth
RMSE	Root Mean Squared Error, m
SD	Stem Diameter, mm
(x, y)	The 2D image point coordinates, pixel
(X, Y, Z)	The 3D coordinates of a 2D image point, m

below the ear (Mantilla-Perez & Salas-Fernandez, 2017). The common practice of quantifying plant architectural traits is via manual measurements in the field, which are time-consuming, labour-intensive, and human-error-prone. Automated solutions have promising potential to increase the efficiency and efficacy of phenotypic data collection.

For automated indoor plant phenotyping systems, each individual maize plant can be transported to a screening station, and imaged using side-view RGB cameras with controlled background colour, lighting conditions, and view angles. Plant architectural traits such as plant height, leaf number, leaf angle, leaf length, and internode length can be extracted based on the plant image skeleton (Cabrera-Bosquet et al., 2016; Zhang et al., 2017). Additional traits including individual leaf surface area and leaf width can be extracted based on the full 3D plant reconstruction of maize and sorghum, which was acquired by using a depth camera to image a rotating plant (Chaivivatrakul, Tang, Dailey, & Nakarmi, 2014; McCormick, Truong, & Mullet, 2016).

However, it remains a challenge to perform automated phenotyping for maize at plant level under field conditions due to occlusions caused by high plant densities. Early related studies focused on automated individual plant sensing for counting population and measuring inter-plant spacing at early growth stages. Top-viewing RGB imaging was first exploited (Shrestha & Steward, 2003, 2005; Shrestha, Steward, & Birrell, 2004; Tang & Tian, 2008a, 2008b). However, as canopies started to overlap, individual plant detection became considerably challenging in the top-view RGB images. An improvement was achieved to cope with overlapped canopies using depth imaging at V2-V3 stages, and the key idea was to find convex patterns that fitted the plant whorls (Jin & Tang, 2009). Most recent field-based high-throughput ground phenotyping systems also adopted the top-view imaging approach for row crops (Andrade-Sanchez et al., 2014; Bai, Ge, Hussain, Baenziger, & Graef, 2016; Jiang et al., 2018; Underwood, Wendel, Schofield, McMurray, & Kimber, 2017; Virlet, Sabermanesh, Sadeghi-Tehran, & Hawkesford, 2017). Regarding plant architecture, plant height and convex hull volume were extracted on a plot basis.

On the other hand, side-view imaging has been utilised for in-field individual plant detection and phenotyping. By taking advantage of the distinct linear structure of the stems, side-view depth imaging was investigated to detect maize plants of V3-V6 stages (Nakarmi & Tang, 2012, 2014). Depth was used to remove background crop rows, and the resultant binary images were processed to detect stem lines using skeletonisation or 2D Hough transform. The stem detection and localisation accuracies were further improved. For extremely tall sorghum plants which have a similar plant architecture to maize plants, several robotic phenotyping systems were developed to quantify plot-based or phytomer-based traits using stereo 3D imaging (Mueller-Sim, Jenkins, Abel, & Kantor, 2017; Salas-Fernandez, Bao, Tang, & Schnable, 2017; Vijayarangan et al., 2018). Convolutional neural networks (CNNs) were used to detect and segment plant stems and leaves (Baweja, Parhar, Mirbod, & Nuske, 2018; Sodhi, Vijayarangan, & Wettergreen, 2017). The CNN-based methods demonstrated superior efficiency over manual methods, however, the extracted phytomer-based traits (stem width, leaf area, leaf length, and leaf width) showed relatively low accuracy due to the difficulty of labelling sufficient training data, especially for 3D point cloud and volumetric data.

This study investigated the characterisation of maize plant architectural traits using side-view depth imaging and several 3D point cloud processing techniques under relaxed field conditions including increased inter-plant spacing and row spacing. The overall goal was to gain more insight about the utility of using side-view depth imaging for field-based maize plant phenotyping. The specific objectives were to (1) extract plant height, visible leaf angle, plant orientation, and stem diameter from the side-view depth images for maize plants grown in the field and (2) determine the system accuracy using field data from an early stage to full maturity.

This paper is organised as follows. Section 2 describes the 3D point cloud processing pipeline for characterisation of plant architectural traits. In Section 3, the results of quantitative analyses between the image-derived values and the in-field manual measurements are presented. Section 4 provides an in-depth discussion about the utility and limitations of the proposed system, followed by potential improvements. Section 5 concludes the study.

2. Materials and methods

Side-view depth images were collected using a Time-of-Flight (ToF) camera (Kinect V2, Microsoft, Redmond, WA, USA). The

depth image has a relatively high resolution of 512× 424 pixels with a wide field of view (FOV) of 70°× 60°. However, the sensor is not designed for outdoor lighting conditions. To alleviate this issue, data collection was conducted no sooner than 1 h before sunset. The ground near the plants was also captured for establishing a reference 3D plane. A row of 20 maize plants (B73) were planted at the Iowa State University Agricultural Engineering and Agronomy Research Farm with an inter-plant spacing of 0.25 m. Additionally, one border row was planted on each side of the experiment row with a row spacing of 1.5 m. The increased inter-plant spacing aimed to reduce occlusions, and the increased row spacing was to achieve a sufficient spatial field of view with the depth camera. Two depth cameras placed at two height levels (0.7 m and 1.7 m) were used when the plants were taller than the FOV of one camera. The two cameras were vertically oriented and rigidly attached to a vertical camera boom, and their relative pose was calibrated using the stereo calibration method in OpenCV (Bradski & Kaehler, 2000) with the infrared intensity images. The actual camera-to-plant distance was set to 0.8 m; the average spatial resolution on the plant surfaces was approximately 3 mm.

The full 3D point cloud processing algorithm consisted of five steps: preprocessing, skeletonisation, stem line detection, skeleton segmentation, and plant architectural traits extraction. The general strategy was to apply 3D skeletonisation to extract a skeleton graph from the unordered 3D point cloud data, and use 3D Hough line detection to locate individual stems. By analysing the positions and orientations of skeleton segments with respect to the stem lines, stems and leaves were separated and their relations were determined. Point Cloud Library (PCL) (Rusu & Cousins, 2011) was used to develop the algorithm, and the data were processed on a computer with a microprocessor running at 3.5 GHz with 16 GB RAM (Xeon, Intel, Santa Clara, CA, USA).

2.1. *Preprocessing*

A depth image was transformed into a 3D point cloud using the camera projection matrix

$$\begin{bmatrix} X \\ Y \\ Z \end{bmatrix} = \begin{bmatrix} f_x & 0 & c_x \\ 0 & f_y & c_y \\ 0 & 0 & 1 \end{bmatrix}^{-1} \begin{bmatrix} x \\ y \\ d \end{bmatrix}, \quad (1)$$

where

(x, y) = the 2D image point coordinates,
d = the depth value of the 2D image point,
f_x = the focal length along the camera X axis,
f_y = the focal length along the camera Y axis,
c_x = the principal point along the camera X axis,
c_y = the principal point along the camera Y axis, and
(X, Y, Z) = the 3D coordinates of the 2D image point.

The parameters in the projection matrix were obtained with the camera calibration method in OpenCV. The camera coordinate system of the bottom camera was set to the world coordinate system. If two cameras were used, the point cloud generated by the top camera was transformed into the world coordinate system. The world coordinate system was defined as follows: the origin was at the projection center of the bottom camera; the X axis was in the vertical direction of the plant growth, the Y axis was in the direction of the crop row, and the Z axis pointed toward the plants. The background was removed by filtering out points whose Z values were beyond 1.5 m. The resultant point cloud only contained the foreground crop row and the ground. The ground points were detected by fitting a 3D plane with Random Sample Consensus (RANSAC) (Fischler & Bolles, 1981). The detected ground plane served as a reference plane for measuring the plant architectural traits. With the normal direction of the ground plane, the point cloud was rotated around the origin such that the ground plane was parallel to the YZ plane of the world coordinate system. Then any points that were 0.05 m above the YZ plane or completely below the plane were considered as ground and removed.

2.2. *Skeletonisation*

2.2.1. *Initial skeleton graph*

Skeletonisation has been widely used to extract structural and topological information of plants from 2D binary images and 3D data. Here, we focus on skeletonisation of 3D data. In addition to 3D point cloud data for 3D surface representation, other common data structures are volumetric data and polygon mesh. For volumetric data, one conventional skeletonisation method is based on iterative thinning (Palágyi & Kuba, 1998; Pudney, 1998). Because the input data are structured, several templates can be defined for the thinning operation. If a voxel and its neighbors match one of the templates, it is removed. This process is continued until no more voxels can be removed. However, this method is sensitive to noise, and can produce undesired skeleton branches. For polygon mesh, the skeleton is obtained by iterative mesh contraction (Au, Tai, Chu, Cohen-Or, & Lee, 2008; Shapira, Shamir, & Cohen-Or, 2008; Tagliasacchi, Alhashim, Olson, & Zhang, 2012). However, the methods were limited to closed polygon mesh without boundary. Skeleton extraction from point cloud has been proposed (Cao, Tagliasacchi, Olson, Zhang, & Su, 2010; Huang et al., 2013; Wu, Huang, Gong, Zwicker, & Cohen-Or, 2015). These methods relied on an iterative optimisation scheme to contract the 3D points to form skeleton structures. However, the parameters needed to be tuned to obtain desirable results. In addition, the contraction process was often time-consuming for large-size point cloud data.

A simple and effective skeletonisation algorithm was developed based on the side-view point cloud of maize plants. The informative and trustworthy parts of the side-view point cloud were the stems and their connected leaves. Specifically, the regions near leaf collars were important for measuring leaf angle, which was defined as the angle between the stem and the midrib of the leaf blade. Occlusions and overlapped leaves made it an ill-posed problem to extract other leaf-related traits such as leaf length, leaf width, and leaf area. Based on the structure of a maize plant, stems were generally close to vertical, and normal leaf angles were less than 90°. This domain knowledge was utilised to efficiently extract a simple skeleton from the point cloud. The skeletonisation algorithm worked as follows. The point cloud was evenly sliced into thin layers along the plant growth direction (the X axis) using the PassThrough filter in PCL (Rusu, 2010), and

Euclidean clusters (Rusu, 2010) were extracted in each layer (Fig. 1 right). A Euclidean cluster was the counterpart of a connected component in 2D image processing, except that two 3D points were considered connected if their Euclidean distance was less than a threshold. An efficient implementation is available in PCL based on the octree data structure. For each extracted Euclidean cluster, its 3D centroid was computed, and the point closest to the centroid was labelled as the skeleton node for representing the cluster.

To create edges, two skeleton nodes were connected if they satisfied the following conditions: (1) they were in two adjacent layers, and (2) their clusters were spatially connected such that the two clusters belonged to the same Euclidean cluster. Using the above rules, a 3D skeleton graph was created for the point cloud. The skeleton graph might contain cycles which would complicate the structure analysis. Hence, cycles were removed by computing the minimum spanning tree of the initial skeleton graph. Minimum spanning tree is a subset of the skeleton graph edges that connect all the nodes, without cycles and with the minimum sum of edge weights. The edge weight equalled the Euclidean distance between the two connected nodes. The minimum spanning tree was further pruned to remove short branches with less than three nodes. The Boost Graph Library was used for graph-related operations (Siek, Lumsdaine, & Lee, 2002). An initial skeleton graph is illustrated in Fig. 1.

2.2.2. *Skeleton graph refinement*

The initial skeleton graph did not accurately represent the topology of maize shoot system near leaf collars. Because the stem and the leaf near a leaf collar were spatially connected, the sliced Euclidean clusters near the leaf collar contained both stem and leaf (Fig. 2 left). Thus, the skeleton nodes were located between the two organs instead of at the centre of the stem. If such a skeleton was used to compute a leaf angle, it was likely to be overestimated (Chaivivatrakul et al., 2014). Note that any skeletonisation algorithms which seek to find the medial axis would produce a similar topology near a leaf collar. To recover a more accurate skeleton for maize plants, a skeleton refinement step was developed. A leaf collar node was defined as a node with two neighbour nodes above it and with one neighbour node below it (Fig. 2). The sliced Euclidean cluster of the leaf collar node was segmented into two clusters using k-means clustering ($k = 2$). If the distance between the two cluster centroids was larger than a threshold R_{stem}, the leaf collar node was split into two skeleton nodes. In each iteration, the leaf collar nodes were processed from plant base to plant top since the direction of splitting was downward. The refinement step was terminated if there was no leaf collar node left to split. The k-means clustering implementation in OpenCV was used for its robustness (Arthur & Vassilvitskii, 2007). The difference between the initial skeleton graph and the refined one is illustrated in Fig. 2.

2.3. *Stem line detection*

Plant detection was necessary because the number of plants in the point cloud was unknown. Stem extraction from the full 3D model of a single plant was realised by fitting the cylindrical shape of the stem (Chaivivatrakul et al., 2014; McCormick et al., 2016). With the full 3D model, fitting a cylinder in the 3D point cloud proved to be a reliable method for a single plant. However, it was far more challenging to fit cylinders for in-field maize plants because the side-view point cloud only showed one side of the stems with occlusions caused by the canopies. To robustly find 3D stem lines in the point cloud, an iterative 3D Hough transform method was adopted (Dalitz, Schramke, & Jeltsch, 2017). A 3D line was parameterised by a point in a 2D grid on the ground plane, and one of a finite number of line directions evenly distributed on a unit sphere. The length and width of the 2D grid were determined by the minimum and maximum Y and Z coordinates of input point cloud. The grid contained square cells, and the cell size was the user-defined parameter, R_{stem}. Every accumulator bin in the Hough space essentially represented a cylinder parameterised by a 2D point in the grid, a line direction, and the cell size (radius). The number of 3D points that were inside the cylinder was the number of votes received by the associated accumulator bin. Unlike the conventional 2D Hough line detection that only transforms all points once, the 3D Hough line detection process transform the point cloud, extracted a most voted line, and remove the inlier points of the line from the point cloud. This process was iterative until one of the following conditions was met: (1) the

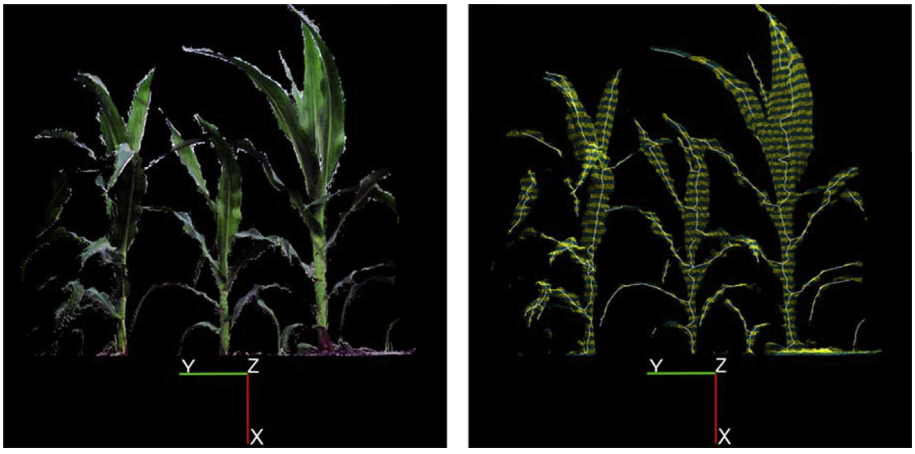

Fig. 1 – Initial skeleton graph. Left: a 3D point cloud after preprocessing. Right: the initial skeleton graph. The alternating colours indicate different slices along the X axis.

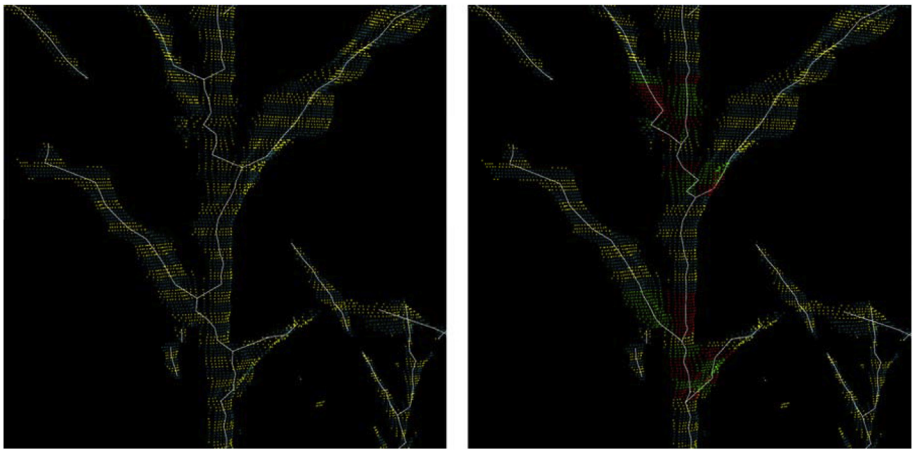

Fig. 2 – Skeleton topology near leaf collars. Left: an initial skeleton graph. Right: the refined skeleton graph. Red and green points indicate the split clusters/nodes.

maximum number of lines was found; (2) the minimum number of votes was not satisfied.

Naively applying the 3D Hough line detection on the point cloud is erroneous and computationally expensive. First, long, straight leaves can lead to false-positive detections. Hough transform is a voting process for the points in the discretised parameter space. The longer, straighter a leaf is, the more votes the passing line obtains. Second, the typical size of a point cloud after preprocessing was in the order of hundreds of thousands. To largely reduce the complexity, the skeleton nodes were used for the Hough transform instead of the raw point cloud. Using skeleton nodes for the Hough transform also reduced the influence of the leaves, which were often wider than stems, and led to more accurate stem line fitting.

For our dataset, the maximum number of lines were set to six, which was more than the maximum number of plants in the point cloud at a time. The minimum vote was determined by

$$\frac{maximum\ canopy\ height}{slice\ thickness} \times 30\%, \tag{2}$$

where the maximum canopy height was the maximum range of point cloud in the plant growth direction (the X axis), and the 30% meant that the 3D line should at least contain inliers in more than 30% of the sliced layers. Often more than one line could be detected for a single plant (Fig. 3). This was solved by grouping the lines, and keeping the one with the most votes in each group. Specifically, the process started with sorting the lines by the number of votes, and accepting the one with the most votes as the first valid stem line. Subsequently, the minimum distance between the next line and each found valid stem line was computed within the range of the ground plane to the maximum height along the X axis. If all distances values were larger than a threshold R_{plant}, the line was accepted as a new valid stem line, and discarded otherwise.

2.4. *Skeleton segmentation*

The skeleton graph contained both stems and leaves, thus their relations to the detected 3D stem lines needed to be solved. The skeleton graph was partitioned into skeleton segments which were one-dimensional subsets of skeleton graph with at least two skeleton nodes, as illustrated in Fig. 4.

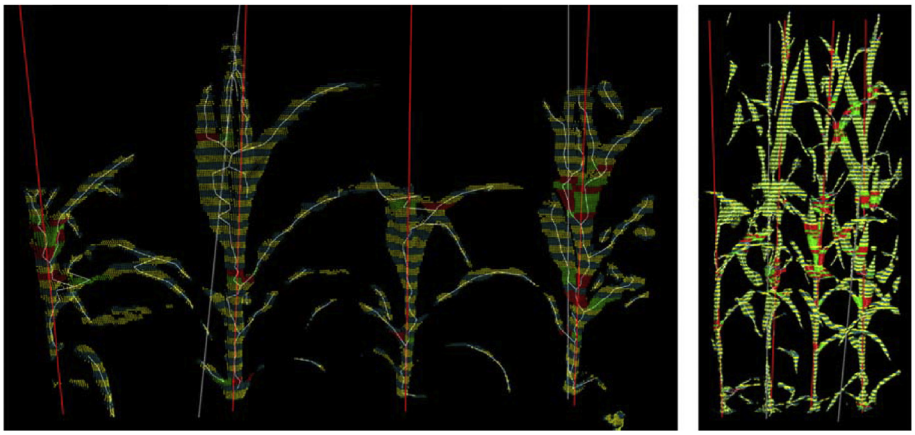

Fig. 3 – Stem line detection. Stem line was detected with 3D Hough line detection of the skeleton nodes. Left: Early stage. Right: Mature stage. Red lines represent valid stem lines. Gray lines are invalid stem lines that have less votes than the closest valid stem lines (best viewed in colour).

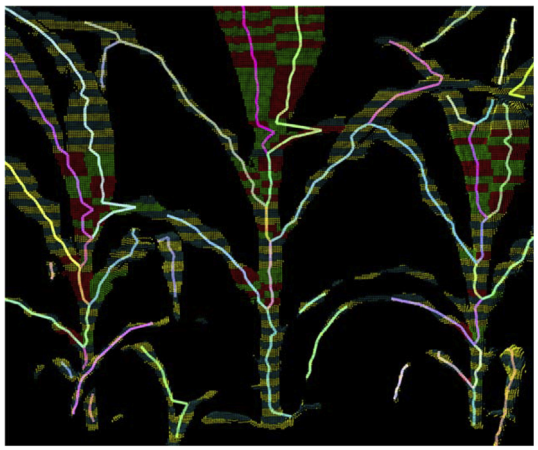

Fig. 4 – Skeleton segments visualised in random colours.

This was achieved by traversing the skeleton graph, starting from skeleton nodes with either one neighbour or at least three neighbours and finishing at skeleton nodes with either one neighbour or at least three neighbours.

Subsequently, the skeleton segments were separated into different groups for the 3D stem lines. The distances between each 3D stem line and the two end nodes of each skeleton segment were computed. If the minimum distance was less than R_{plant}, which was a parameter determined based on the inter-plant spacing, the skeleton segment was assigned to the stem line associated with the minimum distance. Otherwise, the skeleton segment was labelled as an outlier that did not originate from any stem lines. This process completed plant segmentation for the skeleton graph.

2.5. *Plant architectural traits extraction*

Plant architectural traits including plant height (PH), leaf angle (LA), plant orientation (PO), and stem diameter (SD) were extracted based on the detected 3D stem lines and their associated skeleton segments.

2.5.1. *Plant height*

PH can be measured by several different methods, which also depends on the specific growth stage. For instance, PH can be the maximum canopy height or the whorl height before flowering, and tassel apex height or tassel base height after flowering. Based on the observation of our dataset, the whorl and the tassel were typically near the 3D stem line. For the skeleton nodes associated with a 3D stem line, the highest one within a short radius of R_{stem} to the 3D stem line was projected onto the 3D stem line; the distance between the projection and the plant base point was defined as the image-derived PH, where the plant base point was the intersection of the stem line and the ground plane. The PH results are visualised in Fig. 6.

2.5.2. *Leaf angle*

The image-derived LA was defined as the acute angle between a leaf skeleton segment and its associated 3D stem line. Because a leaf was not straight, it was not accurate to use the entire leaf segment to compute LA. Hence, only the skeleton nodes that were within R_{plant} away from the stem line were considered for any skeleton segment. Furthermore, several heuristic rules were implemented to find high-quality leaf skeleton segments. First, a leaf skeleton segment should originate from a stem line. A skeleton segment was not a leaf segment if all the nodes of the skeleton segment were more than R_{collar} distance away from the stem line ($R_{stem} < R_{collar} < R_{plant}$). Second, a leaf skeleton segment should be relatively long. This was enforced by testing the maximum distance between any node of the skeleton segment and the stem line; if the distance was less than R_{plant}, the segment was not a leaf segment. Third, a normal leaf should grow higher than the leaf collar within a short radius of the stem line, and expand away from the stem. Due to occlusions, a skeleton segment could contain both a partial stem and a partial leaf (Fig. 5), which often occurred when the leaves expanded toward the camera. Hence, the skeleton nodes were filtered to keep the ones whose point-to-stem distances were between R_{stem} and R_{plant}. Among the filtered nodes, if the node with the maximum point-to-stem distance was lower than the one with the minimum point-to-stem distance, the segment was not a leaf segment. The leaf orientation was computed using Principal Component Analysis (PCA), and approximated by the first eigenvector of the filtered nodes. Subsequently, the leaf angle was computed with respect to the stem line direction. Lastly, any computed leaf angles outside the range of 10° to 90° were removed. The lower limit aimed to further prevent curved stem skeleton segments being wrongly classified as a leaf skeleton segment, while the upper limit was based on the observation that a normal leaf angle was less than 90° unless it was broken.

2.5.3. *Plant orientation*

Generally, the leaves of a maize plant grow approximately in a plane perpendicularly to the ground plane. Hence, PO was defined as the angle between the plant growth plane and the crop row plane (assumed to be perpendicular to the ground plane). Note that PO was in the range of (−90°, 90°] because −90° and 90° represented the same plant orientation, where the plant growth plane was perpendicular to the crop row

Fig. 5 – Skeleton segments that contain both stems and leaves.

plane. To compute the difference between two PO values, the following equation was used:

$$PO\ Difference\ (a,b) = \begin{cases} a-b-180^\circ, & if\ a-b > +90^\circ \\ a-b+180^\circ, & if\ a-b < -90^\circ \end{cases} \quad (3)$$

For instance, the *PO Difference* (−80°, 90°) equals 10°, while the *PO Difference* (80°, −90°) equals −10°.

To extract the PO value from a detected plant, the skeleton nodes within R_{plant} to the 3D stem line were searched. The intention was to include skeleton nodes on the stem and parts of the leaves nearby. Next, PCA was applied on the 3D coordinates of the found skeleton nodes. Assuming that the first eigenvector corresponded to stem direction, the second eigenvector should correspond to the direction of leaf expansion (PO). The PO value was computed as the angle between and the Y axis (crop row direction) and the projection of the second eigenvector on YZ plane (ground plane) (Fig. 6).

2.5.4. *Stem diameter*

SD was computed for each stem skeleton node. Stem skeleton nodes were found using the following conditions. First, the distance between the node and the stem line was less than R_{stem}. Second, the node had two neighbours, and the first eigenvector computed with the node and its neighbours did not deviate from the stem line by more than 10°. Lastly, the Euclidean cluster associated with the node should not be wider than the maximum possible stem diameter, where the width of the cluster was the range of the cluster in the direction of its first eigenvector.

The SD of a stem skeleton node was computed using the associated Euclidean cluster. Though the cross section of a maize stem may be best approximated by an ellipse, the Kinect V2 depth sensor did not provide a sufficient resolution and repeatability to do so. Hence, SD was approximated by the diameter of the minimum enclosing circle of the point cluster. To obtain a single SD for a plant, the median of the extracted SD values was used (Fig. 6).

2.6. *Experiment*

The data collection started after 30 days after planting (DAP), and was conducted once per week for ten weeks. The imaging

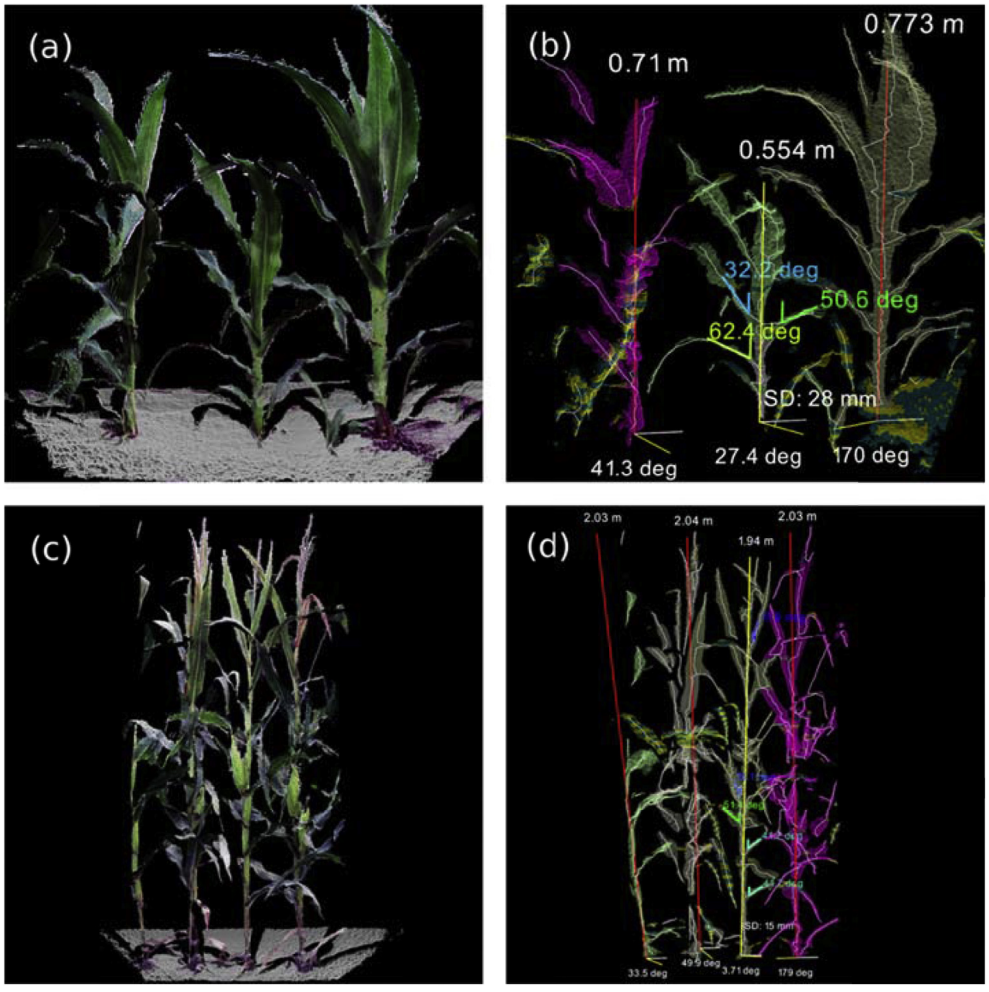

Fig. 6 – Extraction of plant architectural traits. (a) and (c) are the raw point clouds of maize plants at an early stage and a mature stage, respectively. (b) and (d) are the results of plant height (above the stem line), leaf angle, stem diameter (SD), and plant orientation (below the stem line) for the early stage and the mature stage, respectively. Leaf angle and stem diameter were only visualised for the centre plant for clarity. Plant orientation is shifted from (−90°, 90°] to (0°, 180°] for better visualisation.

direction was alternated every week: for odd week numbers, the south side of the crop row was imaged; for even week numbers, the north side was imaged.

2.6.1. *In-field manual measurements*

Manual PH was measured from ground to the highest splitting point between the top two leaves before flowering, and to the tassel apex height after flowering. For LA, one leaf was measured per plant. Before the maize ear was visible, the leaf at the half plant height was measured; after the ear was visible, the leaf above the ear was measured. The corresponding image-derived LA was selected in the extracted results based on the above criteria. PO was measured using a digital protractor, with one leg parallel to the crop row and the other parallel to the horizontal direction of leaf expansion. SD was measured above the first leaf counting from ground when PH was less than 1 m, and at approximately 0.2 m above ground when PH were higher than 1 m. Since the stem cross section was an ellipse, both the major axis and the minor axis were measured using digital callipers, and their average value was used for the evaluation of the image-derived SD.

2.6.2. *Parameter settings*

The same parameter settings were used for the entire dataset. Both the slice thickness and Euclidean clustering threshold were set to 10 mm. Branches with less than three nodes were removed during pruning. R_{stem} was set to 20 mm, which was approximately the average stem diameter across all growth stages. R_{collar} was set to twice of R_{stem} since a leaf collar skeleton node was farther away from the stem line than the stem skeleton node was. R_{plant} was set to 0.1 m considering that the inter-plant spacing was 0.25 m. For each plant, the median of the image-derived SD values within 0.2 m above ground was used for validation, which was found more robust than using the SD of a single stem skeleton node at certain height.

3. Results

This section presents the quantitative analyses between the image-derived plant architectural traits and the in-field manual measurements. Multiple plants were detected in a single point cloud, and the results extracted from the centre plant were used for the analyses. The numbers and reasons of failure cases are reported as well.

3.1. *Plant height*

The algorithm extracted PH for 189 out of the 200 data points (94.5%) from 30 to 93 DAP. The remaining 11 data points could not be used due to considerable short plants before 58 DAP (8), and one dead plant after 72 DAP (3). The image-derived PH achieved a strong correlation with the in-field manual measurements both before flowering (R^2 0.964, RMSE 0.088 m) and after flowering (R^2 0.827, RMSE 0.058 m) (Fig. 7 left). Before flowering, the image-derived PH tended to overestimate the true plant height with a mean absolute error (MAE) of 0.15 m, which was due to the erect top leaves growing in the same direction of the stems. Whereas, after flowering, the image-derived PH was more accurate (MAE 0.054 m) with the tassels visible on the top of the stems. Figure 7 (right) shows the absolute error distributions of the image-derived PH at ten time points, demonstrating relatively large errors from 30 to 58 DAP and small errors from 65 to 93 DAP. Occasionally, extreme errors occurred due to the top canopies of neighbouring plants being wrongly classified as part of the plant of interest, for instance, the maximum absolute errors of 58 DAP and 86 DAP in Fig. 7 (right). This often happened to plants that were much shorter than their neighbours.

3.2. *Leaf angle*

The algorithm extracted LA for 130 out of the 180 data points (72.2%) from 37 to 93 DAP. The data from the rest 50 data points could not be used due to three factors including considerably short plant (S), occlusion (O), and curved stem (C). The number of failed data points for each reason is illustrated in Fig. 8. Among the three factors, the contribution of O increased most over the period. Because the leaf angles were always measured from the same side of the crop row, and the side of imaging was alternated every week, the number of fail data points caused by O increased in a strong fluctuating manner. S and C contributed approximately equally to the issue, however, with less effect than O did. As expected, S mostly occurred at early stages (before 58 DAP) due to late emergence, and caused the failure of stem line detection. When C happened, the distance between the detected stem line and the base of the leaf that required measuring could be too large to be considered as a leaf by the algorithm. C occurred occasionally during the period. On the last data collection date (93 DAP), however, more stems showed curved structures.

For the measurable leaves, a high correlation was observed between the image-derived LA values and the in-field manual measurements (R^2 0.832, RMSE 3.455°) (Fig. 9 left). The slope and intercept of the fit line was 1.0 and 0.96°, respectively, indicating that the image-derived LA was nearly unbiased against the in-field manual measurements. The image-derived LA demonstrated lower errors near the flowering time, indicated by the shorter interquartile lengths and lower median absolute errors of 58 DAP and 65 DAP (Fig. 9 right).

3.3. *Plant orientation*

The algorithm extracted PO for 171 out of the 180 data points (93.8%) from 37 to 93 DAP. The remaining 9 data points were caused by undetected short plants (6), and one dead plant after 72 DAP (3). The error between an image-derived PO value and a manually obtained value was calculated using the *PO Difference* function. Hence, the regression analysis was not performed. The median values of the absolute errors were close throughout the nine time points (Fig. 10 left), with an overall MAE of 13°. For each plant, the distribution of the

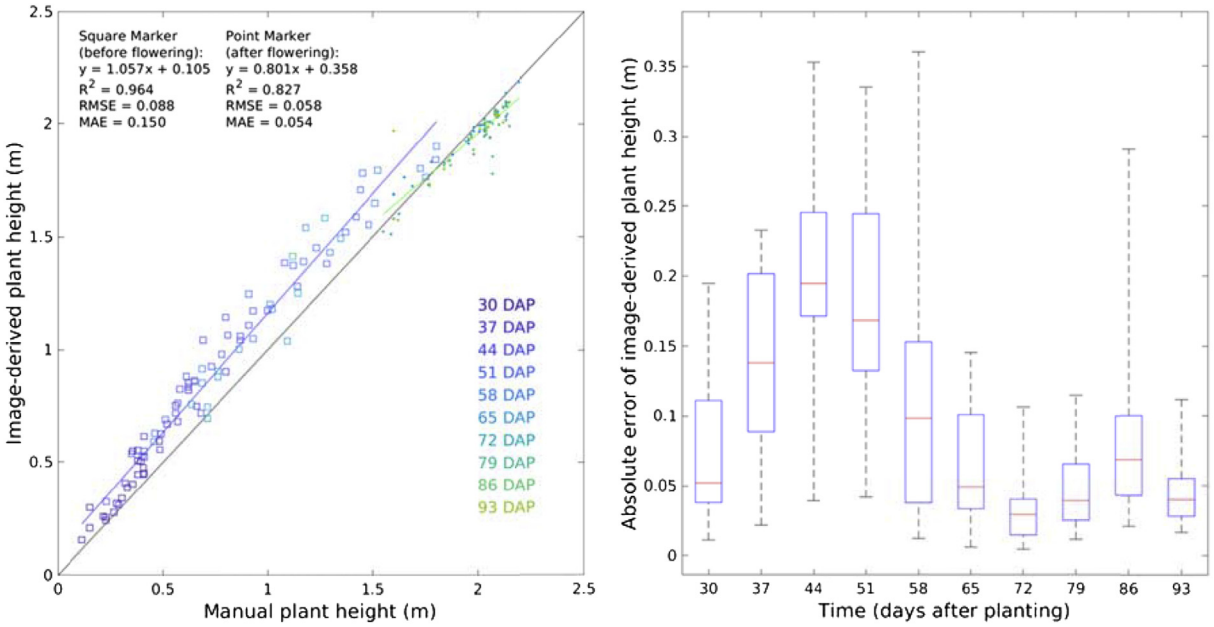

Fig. 7 – Accuracy of the image-derived plant height. Left: Image-derived plant height vs in-field manual measurements. The square markers indicate plants before flowering, while the point markers indicate plants after flowering. The colours represent ten different time points after planting. Right: Absolute errors of the image-derived plant height at ten different time points after planting. The red central mark on each box represents the median, and the bottom and top edges of the box represent the 25th and 75th percentiles, respectively. The minimum and maximum values are indicated by the whiskers.

manually measured plant orientations at nine time points is presented in Fig. 10 (right), demonstrating how the 20 plants were generally oriented. The PCA-based method assumed that the plant leaves expanded approximately in the same plane, which was accurate for most cases. However, the leaves of some plants showed a spiral pattern, leading to some large errors in plant orientation estimation such as the maximum absolute error of 72 DAP (Fig. 10 left).

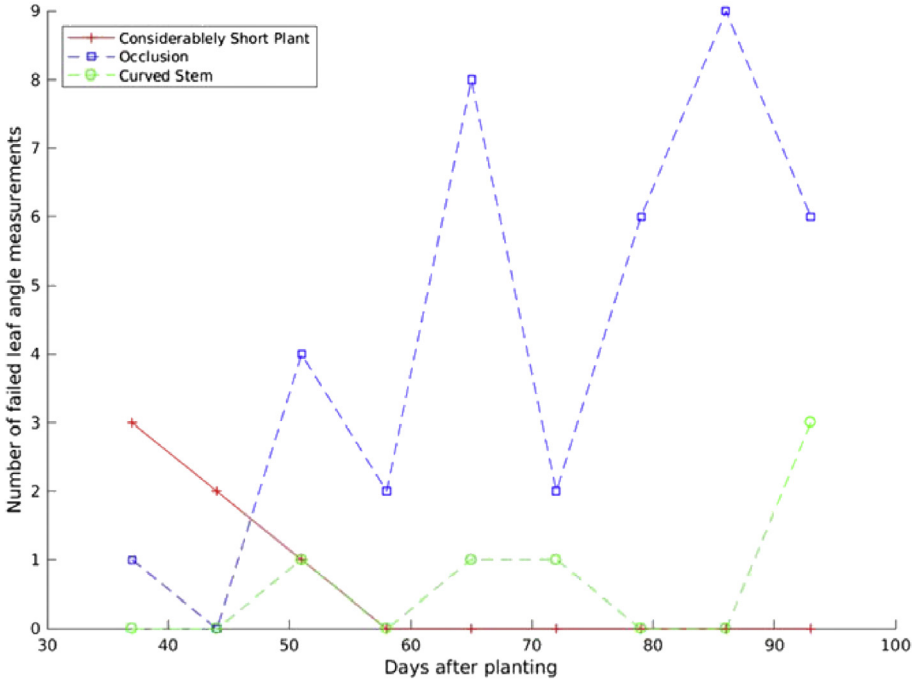

Fig. 8 – Frequency of the failed leaf angle measurements over ten time points. The failure reasons are considerably short plant, occlusion, and curve stem.

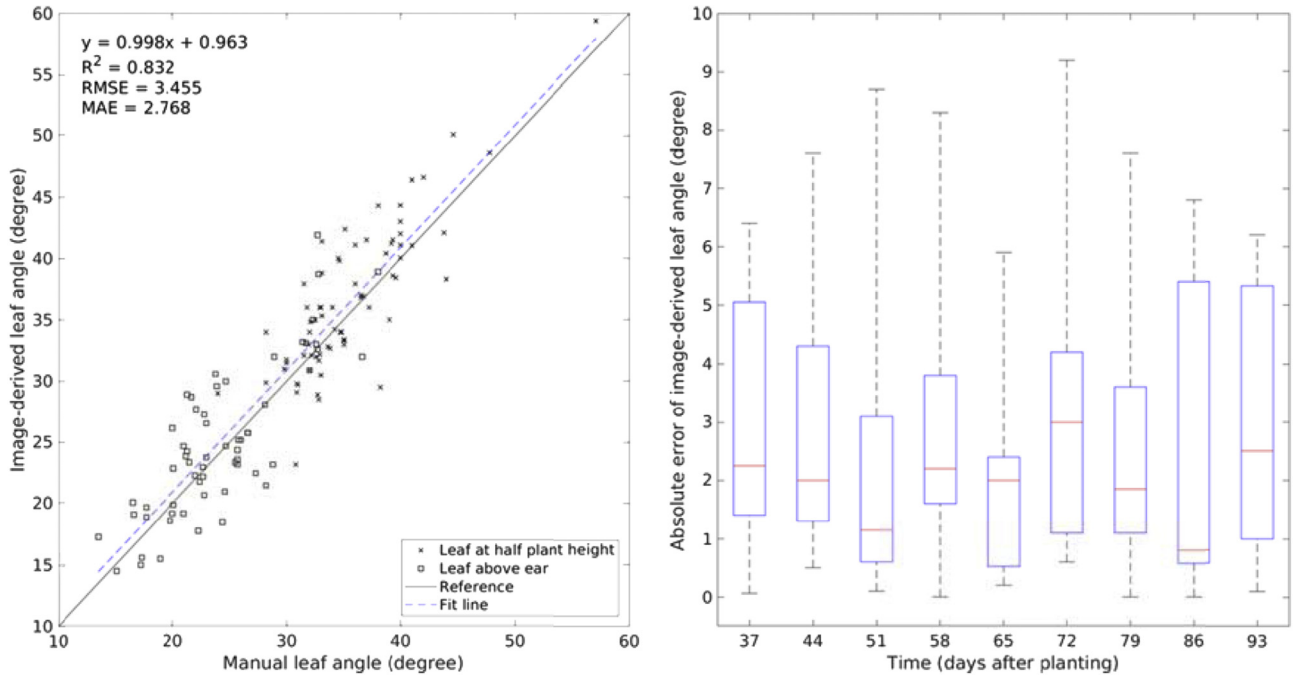

Fig. 9 – Accuracy of the image-derived leaf angle. Left: Image-derived leaf angle vs in-field manual measurements. Right: Absolute errors of the image-derived leaf angle at nine different time points after planting. The red central mark on each box represents the median, and the bottom and top edges of the box represent the 25th and 75th percentiles, respectively. The minimum and maximum values are indicated by the whiskers. (For interpretation of the references to colour in this figure legend, the reader is referred to the Web version of this article.)

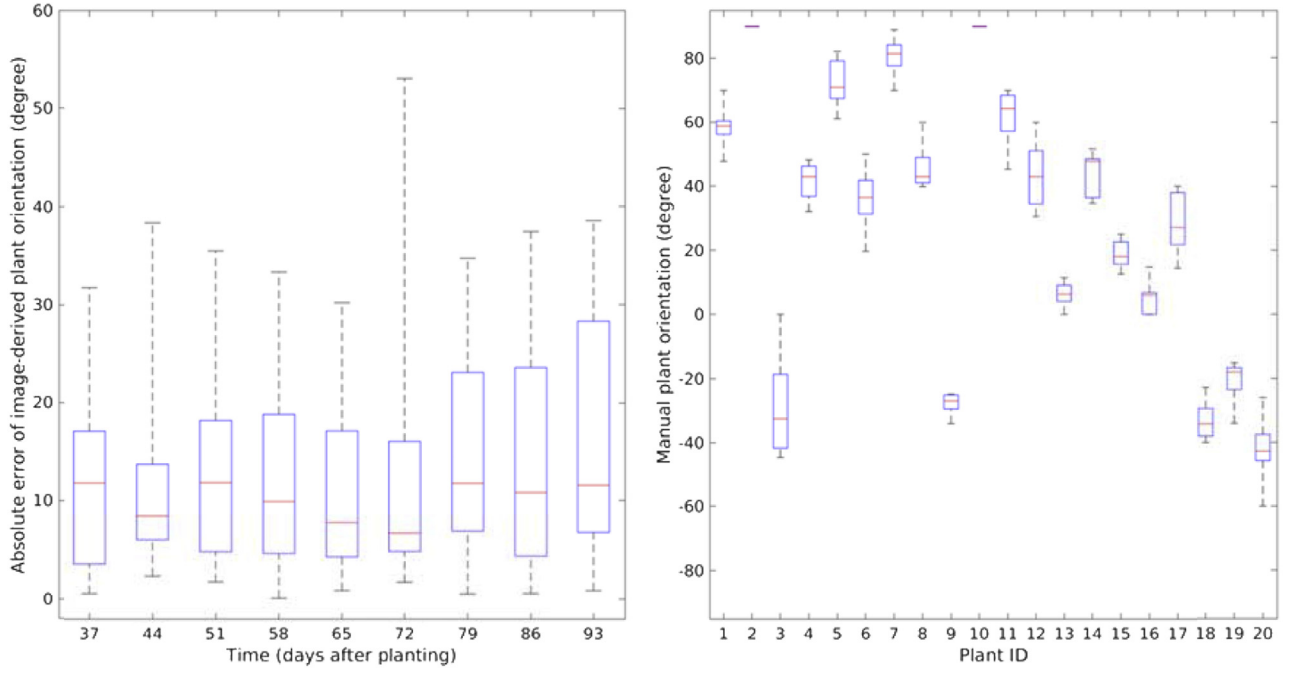

Fig. 10 – Accuracy of the image-derived plant orientation. Left: Absolute errors of the image-derived plant orientation at nine different time points after planting. Right: Distribution of the manually measured leaf angle values at nine time points for each plant. Plant orientation is defined in the range of (−90°, 90°]. The red central mark on each box represents the median, and the bottom and top edges of the box represent the 25th and 75th percentiles, respectively. The minimum and maximum values are indicated by the whiskers. (For interpretation of the references to colour in this figure legend, the reader is referred to the Web version of this article.)

3.4. Stem diameter

The algorithm extracted SD for 180 out of the 200 data points (90%) from 30 to 93 DAP. Among the failed cases, 11 were caused by stem line detection failure. The rest nine were due to the lack of valid stem segments in the skeleton graph, which was largely related to the occlusions caused by the leaves near the plant bases. As expected, the image-derived SD values were moderately correlated with the in-field manual measurements, with R^2 0.27 (Fig. 11 left). The RMSE and MAE were 5.3 mm and 4.4 mm, respectively, which were both relatively large compared to the maximum stem diameter 33 mm. At the early stages, the bottom sections of the leaves were more likely to be considered as stem skeleton nodes due to the shorter internode lengths. This was indicated by the median absolute error of 30 DAP, which was obviously larger than those at later time points (Fig. 11 right).

3.5. Runtime performance

As for runtime, the processing pipeline comprised three major stages: (1) skeletonisation, (2) stem line detection, and (3) feature extraction. The accumulated runtime of each stage for different point cloud sizes is shown in Fig. 12. The point cloud size could also indicate plant growth stage. The runtime of skeletonisation and feature extraction was approximately linear to the input point cloud size, while the runtime of stem line detection was nearly constant around 0.8 s. The runtime of the feature extraction increased faster than that of the skeletonisation with respect to the point cloud size.

4. Discussion

To the best of our knowledge, this is the first study that investigated the utility of using side-view depth imaging to characterise plant architectural trait of maize in the field across a wide range of growth stages, and several important traits including plant height, leaf angle, and plant orientation were accurately quantified at plant level from the 3D point cloud data. The efficacy and efficiency of the processing algorithm relied on the skeletonisation method that effectively reduced the unordered, large point cloud data to a simple graph that preserved the plant architecture. In the following subsections, we discuss the utility, limitations, and potential improvements of some specific aspects of the system.

4.1. Hough transform for 3D stem line detection

This is the first work that 3D Hough line detection was used to detect maize stems in point cloud data. In general, the method worked well for the side-view point cloud from an early stage to full maturity. The detection accuracy largely depended on the amount of stem surfaces that were visible in the point cloud. Plant orientation with respect to the camera could greatly affect the visibility of a stem, which was worst if the leaves expanded toward the cameras. Leaves from adjacent plants could cause occlusions as well. Occlusions could be alleviated by placing more depth cameras to image the same plant from different viewpoints. Multiple synchronised cameras should be preferred to a single moving camera because

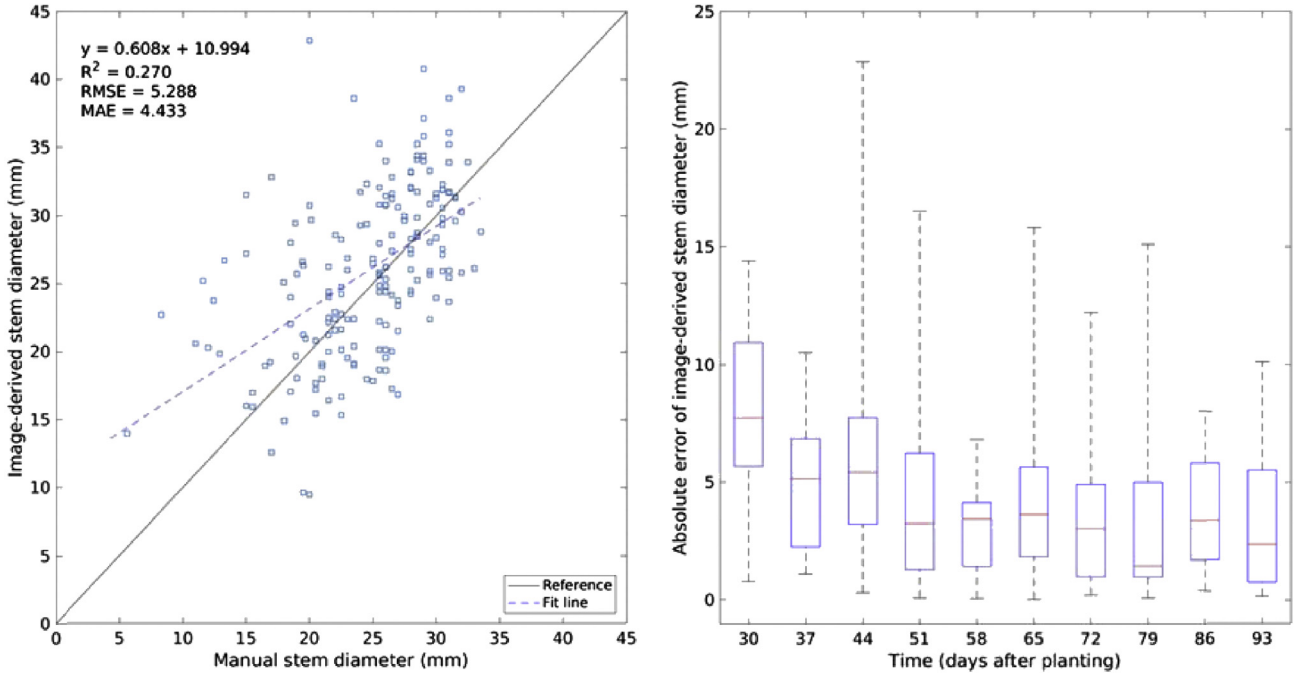

Fig. 11 – Accuracy of the image-derived stem diameter. Left: Image-derived stem diameter vs in-field manual measurements. Right: Absolute errors of the image-derived stem diameter at ten different time points after planting. The red central mark on each box represents the median, and the bottom and top edges of the box represent the 25th and 75th percentiles, respectively. The minimum and maximum values are indicated by the whiskers. (For interpretation of the references to colour in this figure legend, the reader is referred to the Web version of this article.)

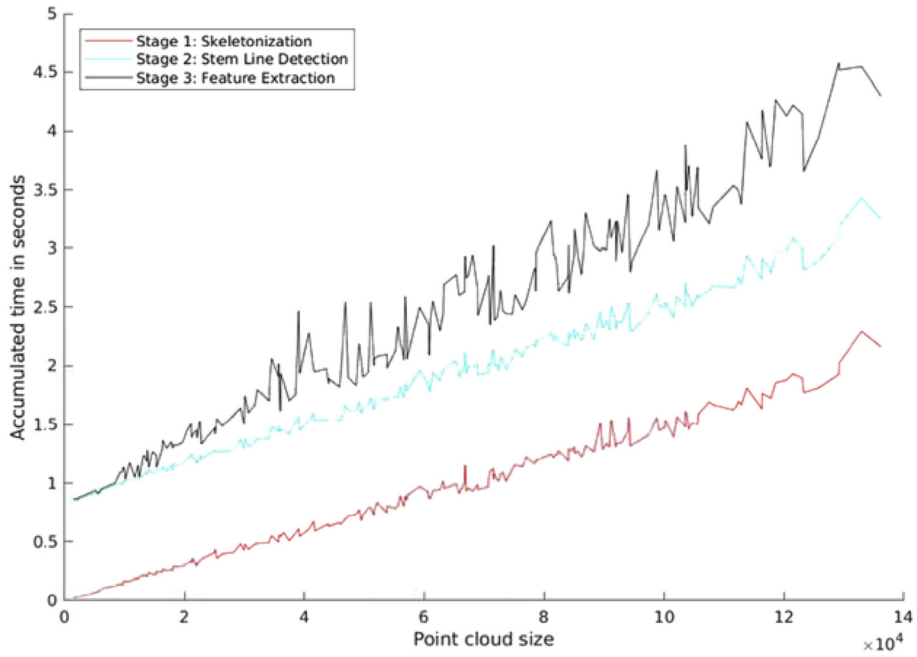

Fig. 12 – Point cloud size vs accumulated time for the three stages of the processing algorithm.

the canopies may move under wind conditions. It will be an important future study to investigate, under common row spacing and inter-plant spacing, the relation between the completeness of the 3D reconstruction of individual maize plants (at least within a short radius to the stems) and the arrangement of multiple side-viewing depth cameras.

Considerably short plants such as late emergers were often missed due to the principle of Hough transform-based detection (Fig. 13). The minimum vote parameter was set based on the height of the maximum height, thus the considerably short plants did not meet the minimum vote requirement. On the other hand, the threshold should not be lowered to accommodate the short because it could increase false-positive detections on long leaves whose orientations were nearly vertical.

It was found that the line-based stem representation has its limitations. A line cannot accurately represent a curved stem, which could occur to some tall plants (Fig. 14). This limitation also affected subsequent traits characterisation because the classification of a skeleton segment depended on its position and orientation with respect to the detected stem line. A potential improvement is to cut the point cloud into multiple layers in the plant growth direction, fit Hough lines in each layer, and obtain a piece-wise linear representation for stems. On the other hand, fitting Hough lines in multiple thinner layers could lead to more errors, especially when vertically orientated leaves were present with the stems partially or completely occluded.

4.2. *Extracted traits*

With a 0.25 m inter-plant spacing, the system achieved accurate estimations for PH, LA, and PO for individual maize plants, and adapted well for multiple growth stages. LA is probably the most important trait characterised by the system. Even though not all leaves could be measured due to occlusions, the extracted leaf angles at different canopy levels could still potentially provide useful information for quantifying a variety's capability to absorb light energy. Furthermore, LA and PO could be possibly utilised to study the interaction between adjacent plants.

The proposed strategy of individual plant segmentation has limitations which could affect the accuracy of image-derived PH. Occasionally, a skeleton segment of a neighbour plant could be wrongly assigned to the plant of interest because the leaf tip happened to be closer to the stem line of

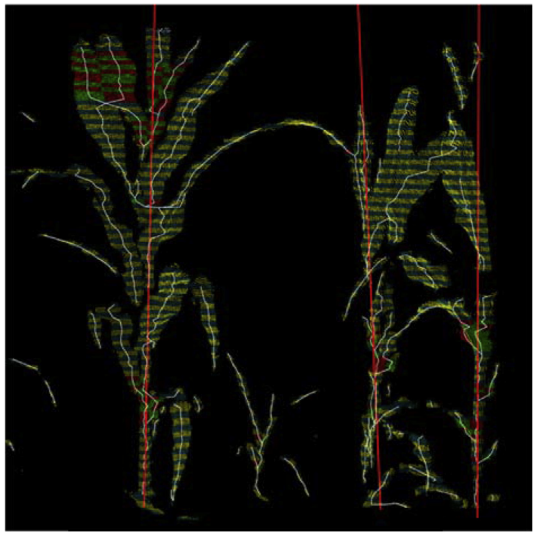

Fig. 13 – Failure of Hough line detection for a considerably short plant.

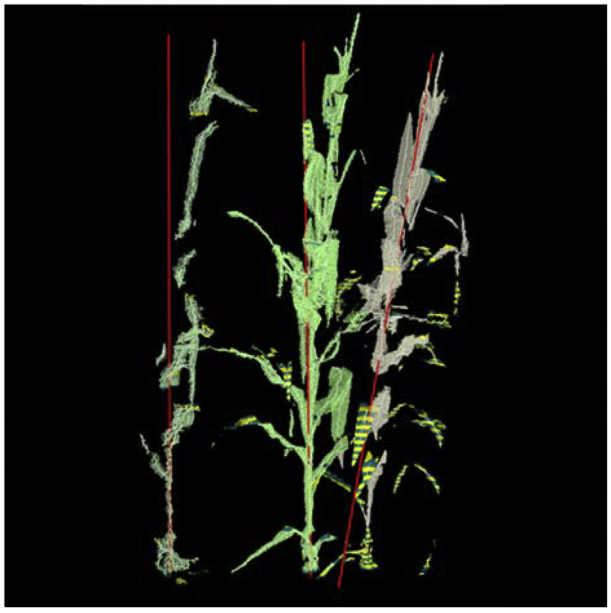

Fig. 14 – Hough lines for curved stems.

the plant of interest than the leaf base was to the stem line of the neighbour.

The long and dense canopies at late growth stages were the primary cause of severe occlusions. Consequently, false negative and false positive detections of leaf segments increased. Though the image-derived LA was found quite accurate, the leaf segment detection rate was not rigorously quantified in this study due to the heavy occlusions. For future research, state-of-the-art CNNs will be used to detect the distinct regions of leaf collars in the RGB-D images acquired by Kinect V2, which could potentially improve the proposed leaf detection strategy.

SD was not accurately quantified by the system. In the following section, an in-depth discussion is provided regarding the reasons for the poor performance of current imaging system for SD estimation, and a potential solution is proposed.

4.3. *Automated instrumentation of maize stem diameter*

The cross section of a maize stem is an ellipse. When covered by leaf sheaths, the stem could appear to be more elliptical. Hence, the image-derived SD measurement is a proxy of the true SD. The manual measurements demonstrated that the stem cross section ellipticity changed over time (Fig. 15), where the ellipticity was defined as the ratio of the major axis to the minor axis, and was estimated by dividing the maximum SD by the minimum SD measured at the same height. Furthermore, from 30 to 50 DAP, the average stem diameter ellipticity decreased from 2.0 to 1.3, and after 50 DAP, the value tended to be constant around 1.3. Only one genotype was used in the experiment, and it is likely that the dynamics of stem diameter ellipticity is not the same for different genotypes.

It is a challenging task to accurately measure maize stem diameter throughout the growing season in an automated and non-destructive way. Stereo vision has been successfully used to measure stem diameter for biomass sorghum in a user-interactive approach, and the results of the genome-wide association studies using the image-derived SD were found consistent with those of a previous study where stems were measured manually (Salas-Fernandez et al., 2017). However, the same approach may not apply to maize. Sorghum tends to grow in higher density than maize. With the higher density, it is

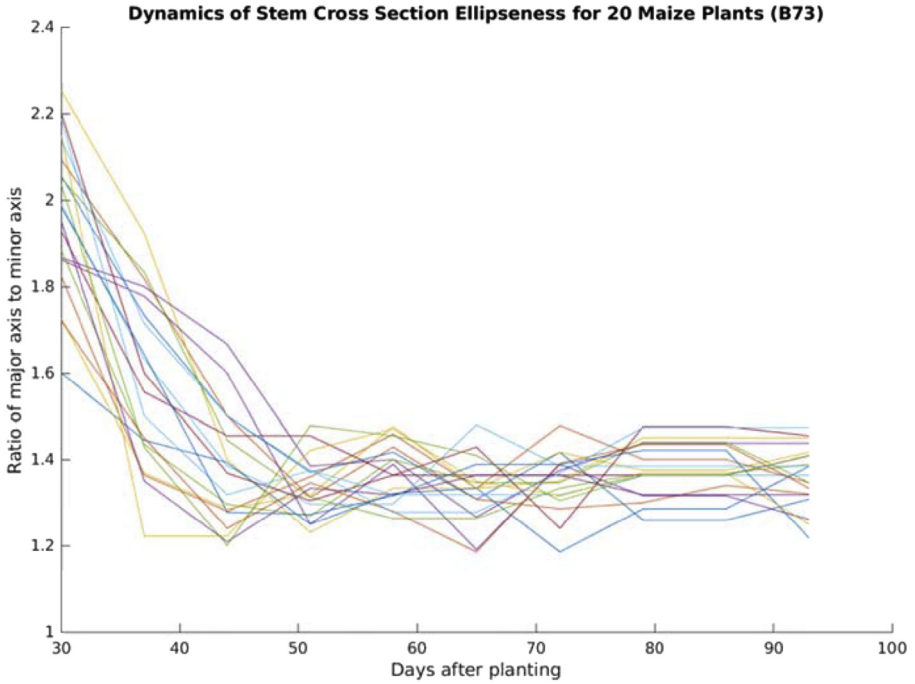

Fig. 15 – Dynamics of the stem cross section ellipticity for the 20 maize plants from 30 to 93 days after planting.

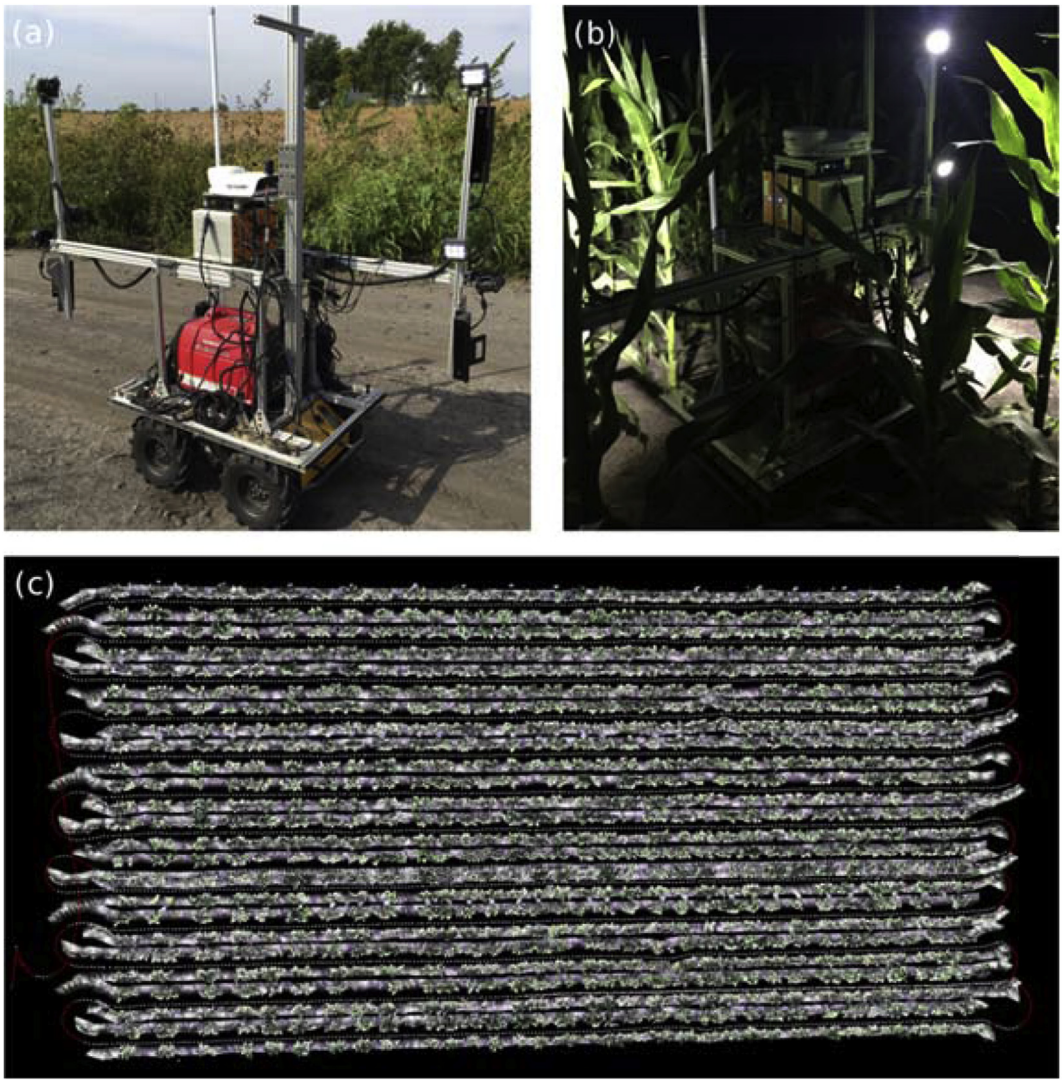

Fig. 16 – Image data acquisition for large field experiments. (a) the robotic data acquisition system, (b) the system collecting side-view depth images at night, and (c) the top view of the stitched 3D point cloud of an entire maize field.

possible that the orientations of sorghum plants are more aligned than those of maize plants. Hence, the SD values of sorghum plants measured in side-view images are approximately along the minor axis of an ellipse. In contrast, lower density could result in higher variation of plant orientation for maize. Plant orientation and camera viewing angle both determine what part of the ellipse is imaged. Additionally, the changing stem diameter ellipticity introduces another unknown variable. Lastly, the measuring point along the stem also matters. The lower half of a stem segment between two adjacent internodes should be measured because the lower half is less affected by the leaf sheath. Typically, a leaf sheath expands outward more and more as it gets closer to the leaf collar.

The solution to automated instrumentation for SD may lie in the fusion of 2D and 3D imaging. There are two aspects that need solving: (1) accurate localisation of stem segments above leaf collars and (2) high-precision 3D surface reconstruction for elliptic cylinder fitting. Again, it is reasonable to believe that maize stem segments can also be accurately located in side-view RGB-D images using state-of-the-art CNNs. As for 3D stem surface reconstruction, current commodity depth cameras lack the required high precision. For example, the precision of stereo cameras and ToF cameras is around 10 mm, whereas, the SD of a mature maize plant is not likely to exceed 50 mm. Typically, short-range high-precision 2D laser profilometers have less than 1 mm repeatability. They have found applications in the manufacturing industry for surface profile inspection. The profilometer only provides depth measurements along a laser line. To create a 3D surface profile, the profilometer needs to be moved during scanning, for instance, using a robotic manipulator. Then, the 3D point cloud can be used to fit an elliptic cylinder which quantifies the cross section of a stem as well as the stem direction.

4.4. Potential for large-scale field experiments

The proposed system provides an efficient and accurate tool to facilitate field-based high-throughput phenotyping for maize plants. The imaging system can be installed on a robotic ground vehicle which navigates between crop rows. In combination with RTK-GPS (Real-Time Kinematic Global Positioning System) data, the side-view point cloud data generated from consecutive depth frames can be registered, and the entire field can be reconstructed (Fig. 16). Accurate registration of the point clouds is challenging even with RTK-GPS and sufficient overlap between image frames because the canopies may be moved by wind or the robot. However, the developed processing algorithm can be used to extract the traits in a single frame, and the results of consecutive frames could be merged based on the positions and orientations of the detected stem lines. This will be further investigated in the future.

5. Conclusions

This study presented a 3D imaging method for field-based maize plant architecture phenotyping. The depth-imaging system was designed to capture side-view 3D point cloud data of the crop row. A point cloud processing pipeline was developed to estimate plant height, leaf angle, plant orientation, and stem diameter across multiple growth stages (V5 to maturity). Plant height estimation was more accurate after flowering, with MAE 0.054 m and R^2 0.83, than it was before flowering, with MAE 0.15 m and R^2 0.96. The image-derived leaf angle achieved MAE 2.8° and R^2 0.83. The occlusions caused by long canopies affect leaf angle extraction more and more as the growth stage proceeded. A definition of plant orientation was introduced along with a method to compute its difference. The MAE of image-derived plant orientation was 13°. These traits could potentially provide valuable information to facilitate genetic studies to improve grain yield for breeders and plant scientists. Though stem diameters were extracted, the accuracy was limited by two factors: (1) the insufficient spatial resolution and precision of the Kinect V2 depth sensor, and (2) the elliptical shape of stem cross section. For future research, we aim to develop a multi-view imaging system to reduce occlusions, and investigate the system performance for commercial inter-plant spacing and different maize genotypes. Another important direction is to characterise the morphological traits regarding maize tassel and ear.

Acknowledgements

This project was funded by the Plant Sciences Institute at Iowa State University. We thank Lisa Coffey (Schnable Laboratory) for her assistance designing and managing the field experiments; Austin Plotz and Taylor Tuel for their assistance in mechanical design and assembly; Qi Mu for her assistance measuring ground truth data.

REFERENCES

Andrade-Sanchez, P., Gore, M. A., Heun, J. T., Thorp, K. R., Carmo-Silva, A. E., French, A. N., et al. (2014). Development and evaluation of a field-based high-throughput phenotyping platform. *Functional Plant Biology, 41*(1), 68–79.

Arthur, D., & Vassilvitskii, S. (2007). k-means++: The advantages of careful seeding. In *Proceedings of the eighteenth annual ACM-SIAM symposium on Discrete algorithms* (pp. 1027–1035). New Orleans, Louisiana:Philadelphia, PA: Society for Industrial and Applied Mathematics.

Au, O. K.-C., Tai, C.-L., Chu, H.-K., Cohen-Or, D., & Lee, T.-Y. (2008). Skeleton extraction by mesh contraction. *ACM Transactions on Graphics, 27*(3), 44.

Bai, G., Ge, Y., Hussain, W., Baenziger, P. S., & Graef, G. (2016). A multi-sensor system for high throughput field phenotyping in soybean and wheat breeding. *Computers and Electronics in Agriculture, 128*, 181–192.

Baweja, H. S., Parhar, T., Mirbod, O., & Nuske, S. (2018). StalkNet: A deep learning pipeline for high-throughput measurement of plant stalk count and stalk width. Field and service robotics. *Springer Proceedings in Advanced Robotics, 5*, 271–284.

Bradski, G., & Kaehler, A. (2000). OpenCV. *Dr. Dobb's Journal of Software Tools, 3*.

Cabrera-Bosquet, L., Fournier, C., Brichet, N., Welcker, C., Suard, B., & Tardieu, F. (2016). High-throughput estimation of incident light, light interception and radiation-use efficiency of thousands of plants in a phenotyping platform. *New Phytologist, 212*(1), 269–281.

Cao, J., Tagliasacchi, A., Olson, M., Zhang, H., & Su, Z. (2010). Point cloud skeletons via laplacian based contraction. In *Shape Modeling international (SMI 2010)* (pp. 187–197). Aix-en-Provence, France: Piscataway, NJ: IEEE.

Chaivivatrakul, S., Tang, L., Dailey, M. N., & Nakarmi, A. D. (2014). Automatic morphological trait characterization for corn plants via 3D holographic reconstruction. *Computers and Electronics in Agriculture, 109*, 109–123.

Dalitz, C., Schramke, T., & Jeltsch, M. (2017). Iterative Hough transform for line detection in 3D point clouds. *Image Processing On Line, 7*, 184–196.

Duvick, D. N., Smith, J. S. C., & Cooper, M. (2004). Long-term selection in a commercial hybrid maize breeding program. *Plant Breeding Reviews, 24*(2), 109–152.

Fischler, M. A., & Bolles, R. C. (1981). Random sample consensus: A paradigm for model fitting with applications to image analysis and automated cartography. *Communications of the ACM, 24*(6), 381–395.

Huang, H., Wu, S., Cohen-Or, D., Gong, M., Zhang, H., Li, G., et al. (2013). L1-medial skeleton of point cloud. *ACM Transactions on Graphics, 32*(4), 61–65.

Jiang, Y., Li, C., Robertson, J. S., Sun, S., Xu, R., & Paterson, A. H. (2018). GPhenoVision: A ground mobile system with multi-modal imaging for field-based high throughput phenotyping of cotton. *Scientific Reports, 8*(1), 1213.

Jin, J., & Tang, L. (2009). Corn plant sensing using real-time stereo vision. *Journal of Field Robotics, 26*(6–7), 591–608.

Mantilla-Perez, M. B., & Salas-Fernandez, M. G. (2017). Differential manipulation of leaf angle throughout the canopy: Current status and prospects. *Journal of Experimental Botany, 68*(21–22), 5699–5717.

McCormick, R. F., Truong, S. K., & Mullet, J. E. (2016). 3D sorghum reconstructions from depth images identify QTL regulating shoot architecture. *Plant Physiology, 172*(2), 823–834.

Mueller-Sim, T., Jenkins, M., Abel, J., & Kantor, G. (2017). The robotanist: A ground-based agricultural robot for high-throughput crop phenotyping. In *Robotics and automation*

(ICRA), 2017 IEEE international conference on (pp. 3634–3639). Marina Bay Sands, Singapore: Piscataway, NJ: IEEE.
Nakarmi, A. D., & Tang, L. (2012). Automatic inter-plant spacing sensing at early growth stages using a 3D vision sensor. *Computers and Electronics in Agriculture, 82*, 23–31.
Nakarmi, A. D., & Tang, L. (2014). Within-row spacing sensing of maize plants using 3D computer vision. *Biosystems Engineering, 125*, 54–64.
Palágyi, K., & Kuba, A. (1998). A 3D 6-subiteration thinning algorithm for extracting medial lines. *Pattern Recognition Letters, 19*(7), 613–627.
Pudney, C. (1998). Distance-ordered homotopic thinning: A skeletonization algorithm for 3D digital images. *Computer Vision and Image Understanding, 72*(3), 404–413.
Rusu, R. B. (2010). Semantic 3D object maps for everyday manipulation in human living environments. *KI-Künstliche Intelligenz, 24*(4), 345–348.
Rusu, R. B., & Cousins, S. (2011). 3d is here: Point cloud library (pcl). In *Robotics and automation (ICRA), 2011 IEEE international conference on* (pp. 1–4). Shanghai, China: Piscataway, NJ: IEEE.
Salas-Fernandez, M. G., Bao, Y., Tang, L., & Schnable, P. S. (2017). A high-throughput, field-based phenotyping technology for tall biomass crops. *Plant Physiology, 174*(4), 2008–2022.
Shapira, L., Shamir, A., & Cohen-Or, D. (2008). Consistent mesh partitioning and skeletonisation using the shape diameter function. *The Visual Computer, 24*(4), 249.
Shrestha, D. S., & Steward, B. L. (2003). Automatic corn plant population measurement using machine vision. *Transactions of the ASAE, 46*(2), 559–565.
Shrestha, D. S., & Steward, B. L. (2005). Shape and size analysis of corn plant canopies for plant population and spacing sensing. *Applied Engineering in Agriculture, 21*(2), 295–303.
Shrestha, D. S., Steward, B. L., & Birrell, S. J. (2004). Video processing for early stage maize plant detection. *Biosystems Engineering, 89*(2), 119–129.
Siek, J., Lumsdaine, A., & Lee, L.-Q. (2002). *The boost graph library: User guide and reference manual*. Boston: Addison-Wesley Professional.
Sodhi, P., Vijayarangan, S., & Wettergreen, D. (2017). In-field segmentation and identification of plant structures using 3D imaging. In *Intelligent robots and systems (IROS), 2017 IEEE/RSJ international conference on*. Vancouver, Canada: Piscataway, NJ: IEEE.
Tagliasacchi, A., Alhashim, I., Olson, M., & Zhang, H. (2012). Mean curvature skeletons. *Computer Graphics Forum, 31*, 1735–1744.
Tang, L., & Tian, L. (2008a). Plant identification in mosaicked crop row images for automatic emerged corn plant spacing measurement. *Transactions of the ASABE, 51*(6), 2181–2191.
Tang, L., & Tian, L. (2008b). Real-time crop row image reconstruction for automatic emerged corn plant spacing measurement. *Transactions of the ASABE, 51*(3), 1079–1087.
Underwood, J. P., Wendel, A., Schofield, B., McMurray, L., & Kimber, R. (2017). Efficient in-field plant phenomics for row-crops with an autonomous ground vehicle. *Journal of Field Robotics, 34*(6), 1061–1083.
Vijayarangan, S., Sodhi, P., Kini, P., Bourne, J., Du, S., Sun, H., et al. (2018). High-throughput robotic phenotyping of energy sorghum crops. *Field and Service Robotics, 5*, 99–113.
Virlet, N., Sabermanesh, K., Sadeghi-Tehran, P., & Hawkesford, M. J. (2017). Field scanalyzer: An automated robotic field phenotyping platform for detailed crop monitoring. *Functional Plant Biology, 44*(1), 143–153.
Wu, S., Huang, H., Gong, M., Zwicker, M., & Cohen-Or, D. (2015). Deep points consolidation. *ACM Transactions on Graphics, 34*(6), 176.
Zhang, X., Huang, C., Wu, D., Qiao, F., Li, W., Duan, L., et al. (2017). High-throughput phenotyping and QTL mapping reveals the genetic architecture of maize plant growth. *Plant Physiology, 173*(3), 1554–1564.